Conjugate heat transfer analysis of a surface air-cooled oil cooler (SACOC) installed in a turbofan by-pass duct

Matteo Gelain, Alexandre Couilleaux, Marc Errera, Ronan Vicquelin, Olivier Gicquel

Conjugate heat transfer analysis of a surface air-cooled oil cooler (SACOC) installed in a turbofan by-pass duct

M. Gelain*
Safran Aircraft Engines, Moissy-Cramayel, France, 77550
ONERA, Châtillon, France, 92320
Laboratoire EM2C, CNRS, École CentraleSupélec, Université Paris-Saclay, Gif-sur-Yvette, France

A. Couilleaux†
Safran Aircraft Engines, Moissy-Cramayel, France, 77550

M. Errera‡
ONERA, Châtillon, France, 92320

R. Vicquelin§
Laboratoire EM2C, CNRS, École CentraleSupélec, Université Paris-Saclay, Gif-sur-Yvette, France

O. Gicquel¶
Laboratoire EM2C, CNRS, École CentraleSupélec, Université Paris-Saclay, Gif-sur-Yvette, France

Surface air-cooled oil coolers (SACOC) are one of the reference technologies adopted in modern turbofan engines to meet the lubricant-cooling requirements. Installed in the by-pass duct, the SACOC are usually composed of a series of staggered fins dissipating the heat load of the engine oil through forced convection with the by-pass flow. Due to the pressure drop generated by the SACOC, which reduces the propulsive thrust of the engine, the performances of the heat exchanger need to be carefully analyzed. Experimentally, several studies have been carried out in wind tunnel test rigs, yet real engine flow conditions, which have a strong influence on the behavior of the SACOC, are arduous to reproduce. The objective of this work is to identify the most relevant integration effects on a finned surface heat exchanger as well as to understand how these effects should be properly replicated in experiments. To do so, conjugate heat transfer simulations are performed in two different configurations. In the former, the SACOC is installed on the outer fixed structure of a turbofan by-pass duct. In the latter configuration, the heat exchanger is mounted on a simple square wind tunnel and the inlet boundary conditions are extracted from the first simulation with different degrees of representativeness. Results obtained with the two configurations are compared, allowing us to assess the most significant sensitivities of the SACOC to engine integration effects.

I. Nomenclature

a_f	=	Thermal diffusivity, m^2/s
AOHE	=	Air-oil heat exchanger
BPD	=	By-pass duct
C_D	=	Drag coefficient
D_f	=	Mesh Fourier number
e	=	Thickness of SACOC platform
H	=	SACOC height

*matteo.gelain@safrangroup.com
†alexandre.couilleaux@safrangroup.com
‡marc.errera@onera.fr
§ronan.vicquelin@centralesupelec.fr
¶olivier.gicquel@centralesupelec.fr

H_{WT} = Wind tunnel's height
IFS = Inner fixed structure
K_f = Thermal conductance, $\mathrm{W}/(\mathrm{m}^2\,\mathrm{K})$
L_{base} = Length of SACOC base
L_p = Length of SACOC platform
M = Mach number
Nu = Nusselt number
Pr = Prandtl number
Pr_t = Turbulent Prandtl number
q = Heat flux, W/m^2
OFS = Outer fixed structure
OGV = Outlet guide vane
R = Specific gas constant, $\mathrm{J}/(\mathrm{kg}\,\mathrm{K})$
RANS = Reynolds-averaged Navier-Stokes
SACOC = Surface air-cooled oil cooler
S_{fin} = Separation between SACOC fins
T = Temperature, K
W = SACOC thickness
α_f = Coupling coefficient, $\mathrm{W}/(\mathrm{m}^2\,\mathrm{K})$
γ = Heat capacity ratio
Δt_c = Coupling period, s
Δy = Size of first mesh cell, m
θ = Non-dimensional temperature
Θ = Azimuth angle
λ = Thermal conductivity, $\mathrm{W}/(\mathrm{m}\,\mathrm{K})$
ν = Inward pointing unit normal
$\Omega_{s/f}$ = Solid/Fluid domain
$\partial\Omega_{s/f}$ = Interface of fluid/solid domain

II. Introduction

The increasing architectural complexity of modern high by-pass ratio turbofan engines poses severe technological challenges with regard to the lubricant cooling as the demand of heat removal capacity keeps growing [1]. Several common oil-cooling strategies are based on the engine air stream as a cold heat sink with a heat exchanger (usually referred to as Air/Oil Heat Exchanger, AOHE) directly installed in the by-pass duct. An optimized design of such exchangers is of fundamental importance not only due to the heat exchange requirements but also because the pressure loss generated by the aerodynamic blockage of the AOHE has a direct impact on the propulsive thrust of the engine. While traditional plate or tube types of AOHE, as shown, for instance, in [2] and [3], are still commonly used in aircraft engines, in recent years attention has been drawn to Surface Air-Cooled Oil Coolers (SACOC), a type of AOHE which has the potential to introduce lower flow disturbances, thereby reducing the overall impact on the performance of the engine. A typical SACOC (see, for instance, [4] and [5]) is composed of a series of staggered fins aligned with the direction of the main flow. The heat, transferred to the fins through a complex oil circuit located beneath the heat exchanger, is thus dissipated by the by-pass flow through forced convection.

The aerothermal performance of finned heat exchangers has been extensively studied analytically (Kadle and Sparrow [6]), numerically (Jonsson et al. [7], S. Kim et al. [8], M. Kim et al. [9]) and experimentally (Sparrow et al. [10], Lau and Mahajan [11], Wirtz et al. [12]), yet only a few works have investigated the behavior of surface heat exchangers while taking into account the specificity of turbofan by-pass flows. Kim et al. [8] performed a numerical and experimental analysis of the influence of a surface AOHE on the engine performance depending on the location and orientation of the fins while Sousa et al. [13] and Villafane and Paniagua [14] carried out experimental studies of a SACOC integrated on the splitter of a turbofan engine reproducing the transonic and high-swirl conditions of by-pass flows downstream of the fan.

In this work, the numerical conjugate heat transfer (CHT) analysis of a finned SACOC is performed. In CHT, the thermal conduction of a solid domain and the aerodynamics of the flow in which the solid is immersed are solved simultaneously, allowing the examination of the fluid-structure thermal interactions. The aim of the study is to assess

the sensitivity of the performance of a SACOC, in terms of heat exchange and pressure drop, to integration effects and to understand how these effects should be reproduced in low-scale experiments. To achieve this goal, two configurations are explored. In the former, the SACOC is directly installed in the by-pass duct (BPD) of a turbofan on the outer fixed structure (OFS) slightly downstream of the outlet guide vane (OGV): the flow making contact with the heat exchanger is thus characterized by a non-equilibrium boundary layer with residual swirl coming from the fan. In the latter, the SACOC is installed in a square wind tunnel, which is the most common testing configuration: boundary conditions at the inlet are extracted from the engine configuration with different degrees of fidelity. Results obtained with the two configurations are compared, the most relevant installation effects are identified and guidelines are given about the level of representativeness required in surface heat exchanger test rigs to reproduce realistic engine conditions.

The work is organized as follows. In section §III, the numerical setup of the CHT computations is described and details about the boundary conditions applied to the fluid-solid interface are given; in section §IV, the surface heat exchanger adopted in this work is introduced and the two studied configurations are presented; finally, results are shown in section §V, followed by the conclusions in §VI.

III. Numerical method

A. Conjugate heat transfer approach and algorithm

In the present work, CHT is realized via a partitioned approach and a steady-state solution is sought. The fluid and solid domains are treated by two independent codes which exchange the boundary conditions at a common interface until convergence of temperature and heat flux is attained. For the fluid domain, the compressible Reynolds-averaged Navier-Stokes (RANS) equations are solved by the multi-purpose CFD software package *elsA* [15] using a time-marching cell-centered finite-volume scheme. For the solid domain, the steady heat equation is solved by the software package Zset [16] with a finite-element method. Finally, the exchange and interpolation of data between the two solvers is performed by the CWIPI coupling library [17].

In order to obtain a fast steady solution to the aerothermal problem, the CHT is carried out through the basic four-step conventional serial staggered (CSS) algorithm, which is schematically shown in Figure 1. First, the solid solver transfers the boundary conditions computed on the solid side of the interface $\partial\Omega_s$ to the fluid side $\partial\Omega_f$; after receiving these boundary conditions, the fluid solver's time-marching scheme advances over a pre-determined number of iterations (usually referred to as coupling period); then, the new boundary conditions computed on the fluid interface $\partial\Omega_f$ are sent to the solid interface $\partial\Omega_s$; finally, the solid code solves the steady heat equation in its domain and the algorithm is repeated from the first step until convergence.

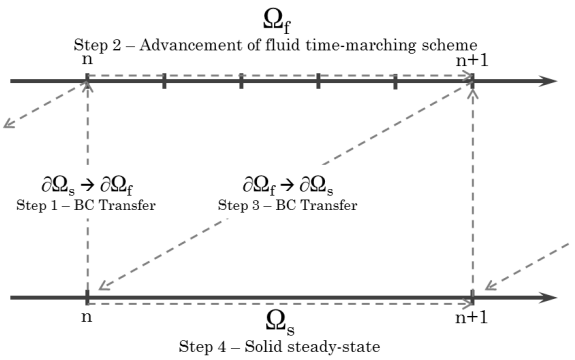

Fig. 1 CSS (Conventional serial staggered) algorithm.

B. Interface treatment

When a partitioned approach is chosen in aerothermal coupling, stability issues can arise at the fluid-solid interface due to the exchange of boundary conditions even in the case where both solvers are intrinsically stable. Consequently, particular attention needs to be paid to the interface treatment in such numerical simulations. The most natural approach

is that of imposing the Dirichlet-Neumann boundary conditions at the fluid-solid interface, that is:

$$\begin{aligned} \hat{q}_s &= -q_f \\ \hat{T}_f &= T_s \,, \end{aligned} \tag{1}$$

where $T_{s/f}$ and $q_{s/f}$ are respectively the temperature and the normal heat flux at the solid and fluid interface; q is computed as $q = -\lambda \partial T / \partial \nu$, where λ is the thermal conductivity and ν is the inward-pointing unit normal; finally, the super-imposed hat symbol ($\hat{\cdot}$) denotes the sought value. These boundary conditions guarantee the continuity of temperature and heat flux between the two domains throughout the simulation. Yet, as shown in [18] with a normal mode stability analysis and an assumption of one-dimensional diffusive fluid-solid transfer, this approach is not unconditionally stable. A straightforward way of improving stability is to add a relaxation coefficient to the first condition in (1), leading to the following Dirichlet-Robin boundary conditions:

$$\begin{aligned} \hat{q}_s + \alpha_f \hat{T}_s &= -q_f + \alpha_f T_f \\ \hat{T}_f &= T_s \,. \end{aligned} \tag{2}$$

On the one hand, the relaxation coefficient α_f plays a positive role on the stability of the coupling and, as shown in [19] and [20] through a one-dimensional Godunov-Ryabenkii stability analysis, a lower stability bound α_f^{min} can be identified, which depends on fluid and solid physical properties as well as on several numerical parameters. On the other hand, α_f can negatively affect the convergence rate if its value is too high. As shown in [21], [19] and [20] through the same Godunov-Ryabenkii stability analysis, a relaxation coefficient α_f^{opt} of compromise between the fast but prone-to-instability coefficients ($\alpha_f \in [\alpha_f^{min}, \alpha_f^{opt}]$) and the stable but over-relaxing coefficients ($\alpha_f \gg \alpha_f^{opt}$) can be expressed as:

$$\alpha_f^{opt} = \frac{K_f}{1 + \sqrt{1 + 2\mathrm{D}_f}} \,, \tag{3}$$

where $K_f = 2\lambda_f / \Delta y$, with λ_f the fluid thermal conductivity and Δy the size of the fluid cell adjacent to the wall, and $\mathrm{D}_f = a_f \Delta t_c / \Delta y^2$, with a_f the fluid thermal diffusivity and Δt_c the coupling period. Interestingly, α_f^{opt} does not depend on any solid physical or numerical properties; furthermore, it is a locally computed coefficient which can assume different values according to the stability requirements of each fluid wall-adjacent cell.

In the present work Dirichlet-Robin conditions (2) are imposed on the fluid-solid interface and the relaxation coefficient (3) is employed. The convergence criterion is based on the infinite norm of the interface temperature with a tolerance equal to 10^{e-03}. Since, as mentioned in section §III.A, the fluid code solves the RANS equations to steady-state with a time-marching scheme, α_f^{opt} is computed taking into account the local time step of the fluid near-wall cells.

IV. Problem description

The study aims at analyzing and comparing the aerothermal behavior of a surface air-oil heat exchanger in two fluid environments, that is the by-pass duct of a turbofan engine and the square tunnel of a typical test bench. The section is organized as follows: in section §IV.A the surface air-cooled oil cooler (SACOC) is introduced and details about geometry, physical properties and boundary conditions are given; section §IV.B is dedicated to the fluid domain and the turbofan by-pass duct (§IV.B.2) and test bench (§IV.B.3) configurations are described in detail.

A. Solid domain: surface air-cooled oil cooler (SACOC)

Figure 2 shows a schematic representation of the geometry of the surface heat exchanger while its characteristic dimensions, normalized with respect to the fin height H, are specified in Table 1.

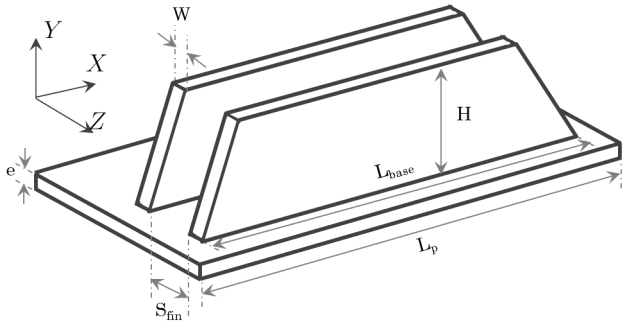

Fig. 2 Schematic representation of two fins of SACOC with dimensions.

Table 1 SACOC's dimensions (normalized with respect to the fin height H).

L_{base}	L_p	H	W	S_{fin}	e
6.67	7.33	1	0.0533	0.133	0.1

The SACOC consists of a series of staggered fins oriented along the direction of the main flow (i.e. the X-axis in Figure 1). The cold sink of the heat exchanger, as mentioned above, is the airstream flowing through the fins; the surface in contact with the air is the CHT fluid-solid interface $\partial\Omega_s$ introduced in section §III.A and its boundary conditions have been extensively described in section §III.B. In practical applications (see [4], for instance), the hot source of the exchanger consists of a complex system of channels and winglets placed beneath the air-fins in which the oil of the engine circuit flows. In this work, in order to simplify the numerical simulations, the oil circuit is not taken into account and the hot source is simply represented by a temperature-imposed surface (with $T_p = 400$ K) situated at the base of a platform of thickness e (see Figure 2).

The inner part of the domain is discretized with an unstructured mesh of around 300,000 nodes per fin; the material is considered to be an isotropic aluminum alloy of constant thermal conductivity $\lambda_s = 150$ W/(m K). The steady-state energy equation is thus reduced to:

$$\nabla^2 T = 0\,, \tag{4}$$

which is solved by the solid solver at every coupling instant.

B. Fluid domain

1. Physical model

For both fluid configurations, the full compressible RANS equations are solved to steady state through an implicit cell-centered second-order time-marching scheme on a structured mesh. The local time step is calculated in every fluid cell with a Courant-Friedrichs-Lewy number CFL = 10 and the fluid-solid coupling takes place every 50 fluid iterations. The fluid is considered to be a calorically perfect gas with heat capacity ratio $\gamma = 1.4$ and specific gas constant $R = 287$ J/(kg K); its dynamic viscosity depends on temperature through the Sutherland law and thermal conductivity is computed with the Prandtl number Pr = 0.72. The contribution of turbulence to the mean flow is taken into account with the two-equation $k - \ell$ model of Smith [22] with a constant turbulent Prandtl number $\mathrm{Pr}_t = 0.9$.

2. Turbofan by-pass duct configuration

The aim of the turbofan configuration is to reproduce the real engine conditions at which a surface heat exchanger normally operates as they may have a strong impact on its performance, in terms of both heat exchange and head losses. For this purpose, a series of 50 fins of the SACOC described in section §IV.A is installed on the outer fixed structure (OFS) of a turbofan by-pass duct (BPD). As shown schematically in Figure 3, the SACOC is placed slightly downstream of the outlet guide vane (OGV).

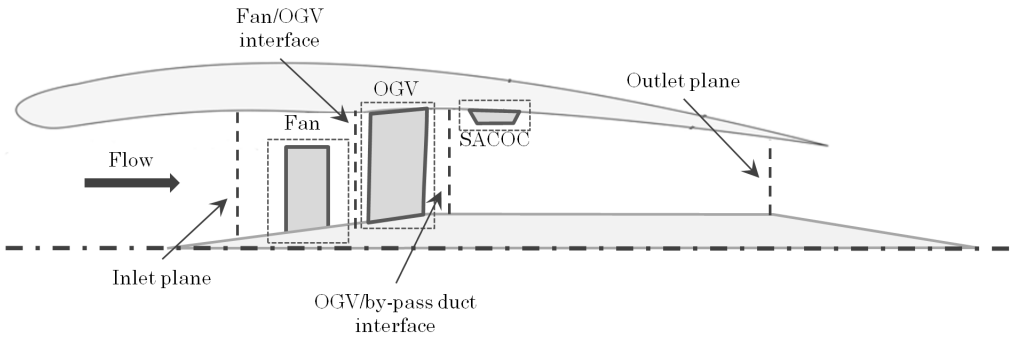

Fig. 3 Schematic cross section of a turbofan by-pass duct with SACOC.

The fluid domain, of which a three-dimensional view is given in Fig. 4, represents an angular sector of the BPD (with azimuthal periodic conditions imposed at the lateral boundaries), wide enough to include one fan/OGV blade. The coordinate system, as shown in Fig. 4, is cylindrical with X representing the engine's axis, R the radial direction (pointing downward so that $R = 0$ on the OFS) and Θ the azimuth. The domain, discretized with a structured mesh of around 60 million nodes, extends from the inlet, situated downstream of the air-intake (which is consequently not simulated) to the outlet, placed at the throat of the nozzle, and can be conceptually divided into three sub-domains:

- Fan sub-domain: in the axial direction it extends from the inlet to the interface with the OGV sub-domain while the azimuth ranges between $\Theta \in [-10°, 10°]$; at the inlet, uniform stagnation pressure and stagnation temperature are imposed, thus neglecting the thickness of the boundary layer originating at the air-intake; the fan blade is completely immersed in the fluid at the center of the domain and an adiabatic no-slip boundary condition is applied at its wall; finally, in order to simulate the rotation of the blade, the steady-state Navier-Stokes equations are solved in a non-inertial frame of reference rotating at the speed of the fan. The fan operates at take-off in standard conditions (*i.e.*, at standard pressure $P_{std} = 101325$ Pa and temperature $T_{std} = 288.15$ K).
- OGV sub-domain: in the axial direction it extends from the rotor-stator interface to the entry of the BPD while $\Theta \in [-4.5°, 4.5°]$; the OGV blade is considered to be an adiabatic no-slip wall; since the blade does not rotate, the frame of reference is Galilean and a simple way of ensuring the communication between the rotor and the stator is that of interposing a mixing-plane [23, 24] which applies a circumferential average of the flow properties. As a consequence, a certain degree of homogenization is introduced into the flow but radial gradients are nevertheless preserved.
- BPD sub-domain: extending from the interface with the OGV sub-domain to the outlet and between $\Theta \in [-4.5°, 4.5°]$, it includes the SACOC, placed on the OFS. Since the mesh requirements of this domain, especially because of the presence of the SACOC fins, are different from those of the OGV domain, the two fluid zones are independently meshed and a non-matching interface, through which flow properties are adequately interpolated, is inserted in between; the SACOC surface is thermally coupled with the solid domain described in §IV.A and the Robin-Dirichlet boundary conditions detailed in §III.B are prescribed; an adiabatic no-slip condition is applied to the remaining surfaces of the by-pass duct; finally, at the outlet, a pressure imposed boundary condition is prescribed ($P_s = P_{std}$).

Due to the presence of the fan and OGV, several aspects of the functioning of a realistic turbofan can be taken into account, such as: the aerodynamic interaction which may occur between the SACOC and the OGV; the impact of the heat exchange and of the pressure drop generated by the heat exchanger on the engine's thrust; the real conditions of the flow making contact with the SACOC fins, *i.e.*, a non-equilibrium boundary layer with residual swirl coming from the fan. In this work, we will be focusing on the latter.

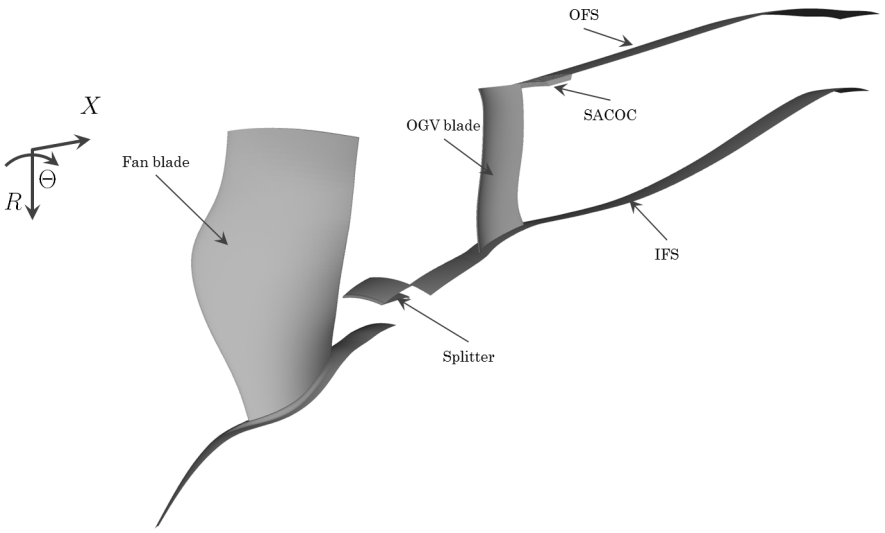

Fig. 4 Three-dimensional view of the turbofan fluid domain.

3. Test bench configuration

Ideally, the performances of a SACOC would always be assessed in its operating environment, in this case a turbofan; however, such full-scale tests are extremely expensive and time-consuming, especially when a great number of heat exchanger designs need to be tested. Consequently, the most common testing configuration still remains the wind tunnel and it is important to understand to which extent such an experimental environment can be representative of the real engine conditions.

The aim of the second configuration studied in this work is, therefore, to analyze the performance of a SACOC in a typical test rig and to compare the results with those obtained with the engine configuration described in section §IV.B.2. The geometry of the test bench, shown in Figure 5, is that of a square wind tunnel of side H_{WT} so that $H/H_{WT} = 0.15$, where H is the SACOC fin height (see §IV.A).

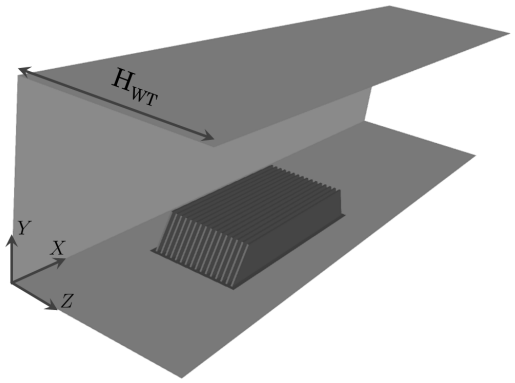

Fig. 5 SACOC implemented in square wind tunnel.

The domain is discretized with a structured mesh of around 30 million nodes and includes 16 fins of the SACOC described in section §IV.A which are placed on the lower wall of the wind tunnel at the same distance from the inlet as the one separating the SACOC and the OGV/BPD interface described in §IV.B.2. At the side walls, as well as at the upper and lower ones, adiabatic no-slip boundary conditions are applied; the SACOC surface is thermally coupled with

the solid domain described in §IV.A and the Dirichlet-Robin boundary conditions detailed in §III.B are prescribed; at the inlet, flow properties computed in the engine configuration §IV.B.2 are extracted from the OGV/BPD interface and applied as boundary conditions. This is done with various levels of complexity, as follows:

- Uniform profiles: at the OGV/BPD interface, the fluid properties (stagnation pressure, stagnation temperature, turbulent kinetic energy and length-scale) are averaged between $R \in [0, H_{WT}]$ and $\Theta \in [-4.5°, 4.5°]$ and imposed at the inlet of the square wind-tunnel. Both radial and azimuthal gradients thus disappear and the flow reaching the SACOC is homogeneous.
- One-dimensional profiles: the fluid properties extracted from the engine configuration are averaged along $\Theta \in [-4.5°, 4.5°]$ for each value of R. While azimuthal gradients vanish, radial gradients are preserved and the SACOC is reached by an average boundary layer.
- Two-dimensional profiles: the boundary conditions are extracted from the OGV/BPD interface and simply interpolated on the wind tunnel's grid without any azimuthal or radial average so that all gradients are preserved. These boundary conditions are meant to reproduce the engine conditions at the highest degree of fidelity.

At the outlet, a pressure imposed boundary condition is prescribed and the pressure is calibrated so that the bulk velocity coincides between the two configurations.

V. Results

A. Engine configuration

In this section the results obtained with the engine configuration described in §IV.B.2 are presented. In the following, the cylindrical coordinate system of Fig. 4 is used. Therefore, the radial direction points towards the axis of the engine and $R = 0$ on the OFS; besides, the azimuth Θ ranges between $[-4.5°, 4.5°]$; the subscript $(\cdot)_{ref}$ indicates a fluid property averaged over the surface of the OGV/BPD interface between $R \in [0, H_{WT}]$ and $\Theta \in [-4.5°, 4.5°]$; finally, $\overline{(\cdot)}$ denotes Reynolds average.

Figure 6 shows the distribution of some flow properties at the OGV/BPD interface. As can be seen, the flow is highly heterogeneous downstream of the OGV, with the distribution of the Mach number (6a) revealing the presence of a strong wake originating at the trailing edge of the OGV blade. Figure 6b, instead, shows the pitch angle α of the velocity vector; it can be seen that two counter-rotating vortexes are generated at the hub and at the tip of the OGV, the latter being particularly significant as a consequence of the ongoing effect of the fan blade slack. Finally, Fig. 6c shows the distribution of the yaw angle β of the velocity vector which, except in proximity of the OGV hub and tip, is essentially negative, showing the presence of residual swirl coming from the fan.

The SACOC fins are therefore reached by a complex, three-dimensional, non-equilibrium flow. The temperature field resulting from the forced convection with this flow, is shown in Fig. 7, with $\theta = \left(\overline{T} - T_{ref}\right) / \left(T_p - T_{ref}\right)$, where T_p the temperature at the base of the SACOC fins (see §IV.A). The temperature distribution is remarkably heterogeneous, with the fins situated on the pressure side of the OGV being significantly colder than those located on the suction side and, especially, in the wake, indicating that certain fins exchange more heat than others.

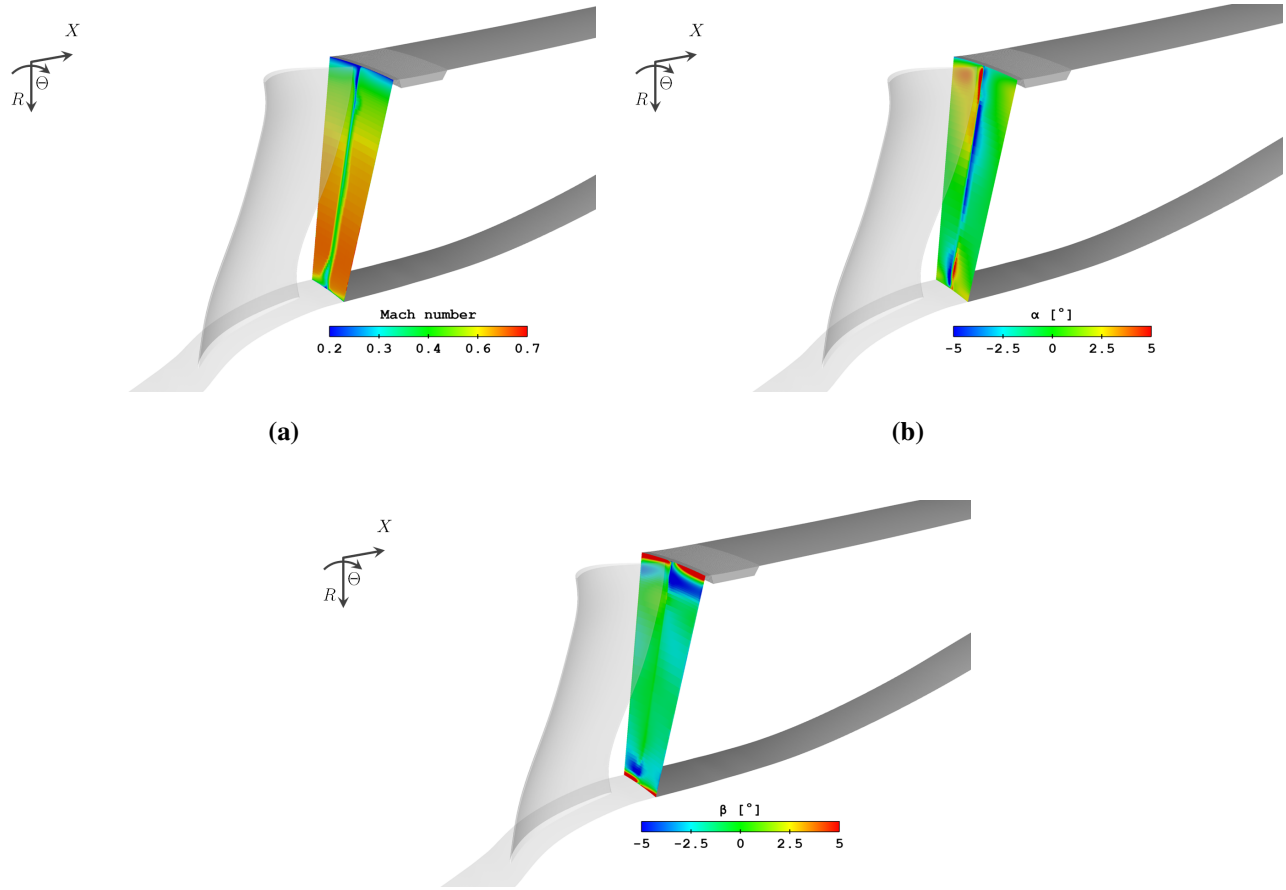

Fig. 6 Characteristics of the flow at the OGV/BPD interface: Mach number (a), pitch (b) and yaw (c) angles of the velocity vector.

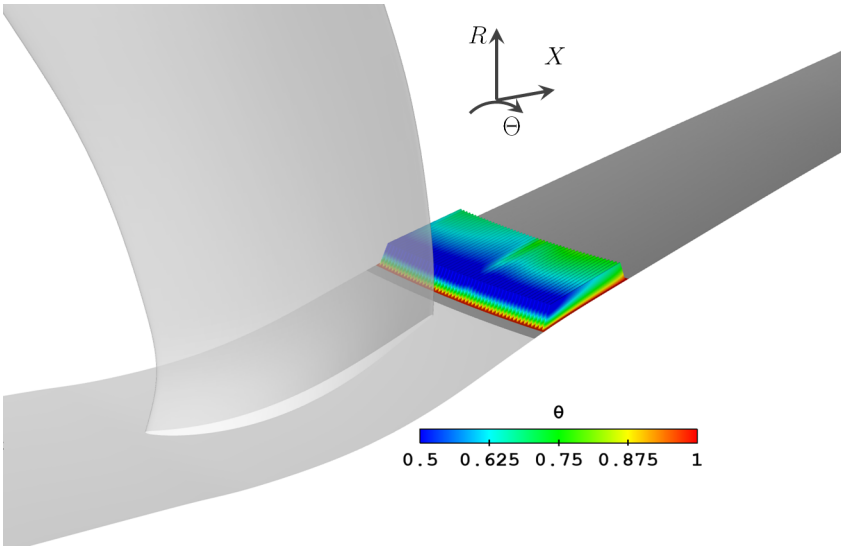

Fig. 7 Non-dimensional temperature field θ on the SACOC fins.

Figure 8a shows the average Nusselt number, computed as $\langle \mathrm{Nu} \rangle = \Phi_w H / \left(\lambda_{ref} \left(T_p - T_{ref}\right)\right)$, fin per fin from the pressure side to the suction side; Φ_w is the wall heat flux averaged over the surface of the fin and H is the fin height. As can be seen, the two central fins, placed behind the trailing edge of the OGV blade, exchange approximately 30% less heat than the best performing fins. It is interesting to compare the distribution of the Nusselt number with that of the drag coefficient $\mathrm{C}_D = \mathcal{T}_w / \left(\frac{1}{2}\rho_{ref} u_{ref}^2\right)$, where $\mathcal{T}_w$ is the wall shear stress averaged over the surface of the fin, which is shown in Fig. 8b. The more heat is exchanged by a fin, the more important is the total viscous drag contributing to the pressure drop. This analogy can be explained by analyzing the distribution of the mass flow rate passing through every channel separating two consecutive fins. In Figure 8c both the entering (by the leading edge) and leaving (by the trailing edge) mass flow rates of every fin are shown, non-dimensionalized with respect to P^t_{ref} and T^t_{ref}, with P^t and T^t the stagnation pressure and temperature, respectively. The distribution of the entering mass flow rate qualitatively resembles those of the Nusselt number and of the drag coefficient, which is intuitive: the more mass flows between two fins, the higher the average speed of the flow is and both the heat exchange and the head losses increase.

It is also interesting to investigate the distribution of the leaving mass flow rate, which actually resembles that of $\langle \mathrm{Nu} \rangle$ and C_D even more than the entering one. For every fin, it can be observed that there is a loss of mass flow between the leading and trailing edges. This can be explained by the fact that the SACOC, because of both its shape and the heat it provides, constitutes an aerodynamic obstacle that the flow prefers to avoid. Therefore, a significant portion of the mass flow escapes from the upper part of the SACOC without crossing its whole length, thereby reducing the thermal efficiency of the fins. On the pressure side of the OGV (left-hand side of Fig. 8c), around 50% of the mass flow rate is lost through the upper side of the fins, yet this phenomenon is exacerbated on the suction side, where, for some fins, less than 30% of the entering mass flow rate attains the trailing edge. Not surprisingly, these fins have among the lowest average Nusselt number and drag coefficient.

A possible explanation for the stronger loss of mass flow on the suction side might be the interaction between the heat exchanger and the vortex generated at the trailing edge of the OGV blade, the sense of rotation of which might help drive the flow away from the SACOC fins. Visualizations of the flow are given in Figure 9. Figure 9a shows the temperature iso-surface $\theta = 0.4$ colored by the Mach number; Figure 9b shows the velocity streamlines on two azimuthal planes $\Theta = 2.25°$ (*i.e.*, on the pressure side of the OGV) and $\Theta = -2.25°$ (*i.e.*, on the suction side of the OGV). As can be seen, on the pressure side the flow remains well attached to the OFS downstream of the SACOC and, while the velocity streamlines do deviate from the fins causing the aforementioned loss of mass flow, the temperature iso-surface adheres to the wall; on the other hand, the suction side is characterized by a stronger deviation of the velocity streamlines with an important flow separation (approximately as high as the SACOC fins and at least twice as long) taking place downstream of the heat exchanger.

Table 2 summarizes the global performance parameters of the SACOC on both the pressure and suction side. The

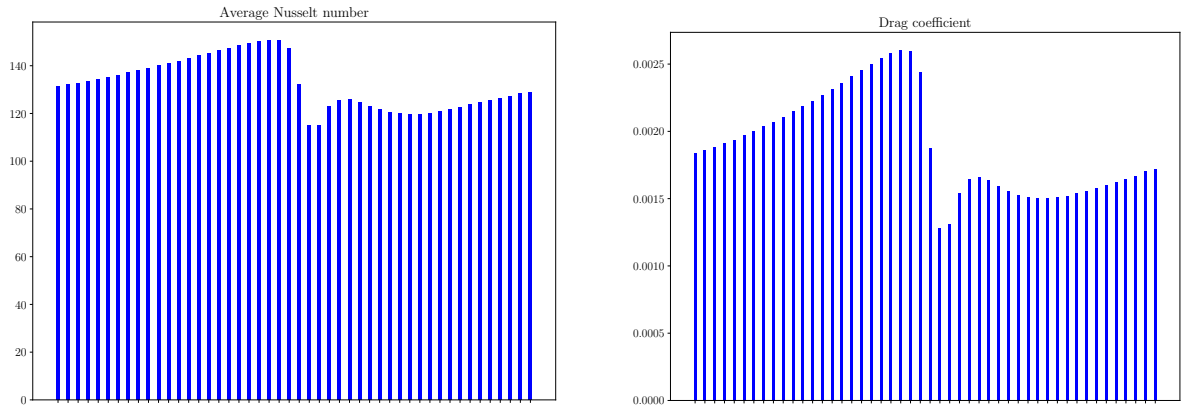

(a)

(b)

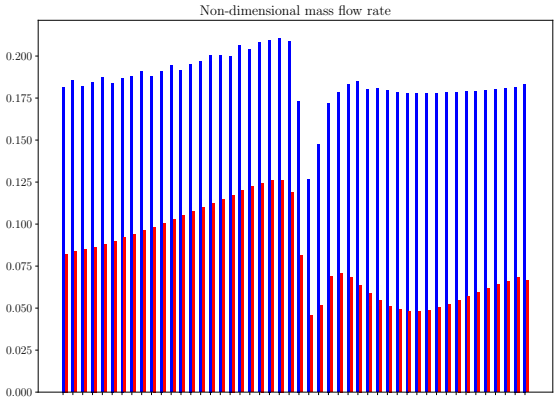

(c)

Fig. 8 Distribution of average Nusselt number (a), drag coefficient (b) and mass flow rate (c) on the 50 SACOC fins, from the pressure side to the suction side of the OGV. For Fig. (c) the blue and red bars represent the entering and leaving mass flow rates, respectively.

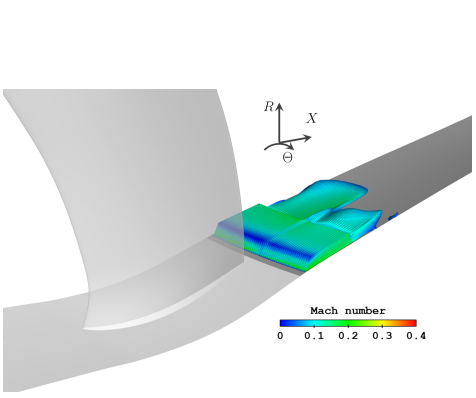

(a)

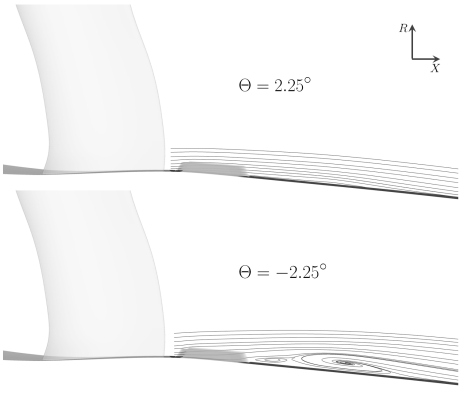

(b)

Fig. 9 Temperature iso-surface $\theta = 0.4$ colored by the Mach number (a) and velocity streamlines on two azimuthal planes at $\Theta \pm 2.25°$ (b).

global Nusselt number and drag coefficient are simply computed by averaging the values of the fins located on each side; the head losses, instead, are calculated between the OGV/BPD interface and a plane located two fin lengths downstream of the SACOC by computing the average stagnation pressure between $\Theta \in [0°, 4.5°]$ for the pressure side and $\Theta \in [-4.5°, 0°]$ for the suction side. As can be seen, despite the drag coefficient being higher for the pressure side fins, the global pressure drop is more important on the suction side. Indeed, the dissipation caused by the skin friction between the fins is only one of the contributions to the head losses and, in this case, the separation bubble shown in Fig. 9 seems to play a much more important role. Therefore, it is possible to conclude that the pressure side of the SACOC is significantly better performing than the suction side since not only is the global heat exchange approximately 15% higher but the global pressure drop is around 70% lower.

Table 2 SACOC's performances in terms of average Nusselt number, drag coefficient and global head losses on the pressure and the suction side of the OGV.

	Pressure side	Suction side	Comparison
$\langle Nu \rangle$	140.1	123.12	+13.7%
C_D	0.0022	0.0016	+37.5%
Head losses	0.7%	2.2%	− 68%

B. Test bench configuration

The objective of this section is to investigate to which extent the performances of a SACOC installed in a turbofan by-pass duct are reproducible in a common test rig configuration like the one introduced in §IV.B.3. In the following, the frame of reference is the one of Fig. 5; therefore, X represents the axial direction, Y the wall-normal direction (with the SACOC installed on the $Y = 0$ wall) and Z the spanwise direction; as shown in §IV.B.3, 16 fins are installed in the wind tunnel; furthermore, as already mentioned, the boundary conditions imposed at the inlet of the test channel are extracted from the OGV/BPD interface of the engine configuration with different levels of complexity. In the next paragraphs, the results obtained with uniform (§V.B.1), one-dimensional (§V.B.2) and two-dimensional (§V.B.3) boundary conditions are presented.

1. Uniform boundary conditions

At the inlet, constant values for the stagnation pressure, stagnation temperature and turbulence are imposed; furthermore, the flow is supposed to be completely axial (*i.e.*, oriented along the X direction, see Fig. 5). Such homogeneous inlet flow conditions are typical of test rigs where the flow reaches the test section after crossing a settling chamber without any further manipulation (see, for instance, [11]). In order for this flow to be somewhat representative, the inlet conditions are extracted from the OGV/BPD interface and averaged between $R \in [0, H_{WT}]$ and $\Theta \in [-4.5°, 4.5°]$.

Figure 10 shows the comparison between the Mach number profiles at the wind tunnel's inlet (averaged along the spanwise direction Z) and at the OGV/BPD interface (averaged along the azimuth Θ). As can be seen, at the inlet the Mach profile is essentially flat, except for a small inflection near $y/H_{WT} = 0$ which is due to the deceleration of the flow running into the aerodynamic blockage of the SACOC. In other words, no boundary layer is injected at the inlet and, with respect to the engine profile, the Mach number is significantly overestimated for $y < H$, where H represents the fin height (see §IV.A).

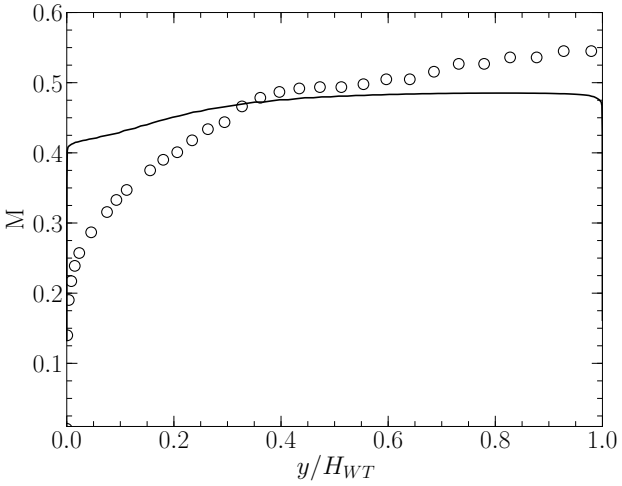

Fig. 10 Uniform boundary conditions. Comparison of Mach number profiles: —— wind-tunnel's inlet with uniform boundary conditions; ○ OGV/BPD interface of the engine configuration.

Figure 11 shows the Nusselt number, drag coefficient and entering as well as leaving mass flow rate for each SACOC fin compared to the results presented in §V.A. The same non-dimensionalization used in §V.A is employed here. As could be expected, all the SACOC fins have a similar behavior (except for a small border effect visible on the mass flow rate distribution) as a consequence of the homogeneous injection. As can be seen, the higher Mach number in the lower part of the wind tunnel leads to a strong overestimation of all the performance parameters. The Nusselt number is around 60% higher compared to the average engine SACOC fin while the drag coefficient is more than 100% more elevated. Concerning the mass flow rate, not only is the entering mass flow over-estimated, yet the ejection event described in §V.A is in this case significantly weaker compared to the engine configuration; indeed, around 30% of the mass flow is lost by the upper part of the SACOC compared to more than 50% for the engine fins.

Thanks to these results, it is possible to conclude that uniform boundary conditions, despite being representative of the mean flow at the OGV/BPD interface, do not allow us to predict any performance parameter of interest of the SACOC. There certainly exists a homogeneous flow capable of reproducing, at least on average, the behavior of the complex, anisotropic flow downstream of the OGV, yet the values to be imposed to the stagnation pressure at the inlet cannot be known *a priori*. In practice, in case where the test rig cannot generate but homogeneous flows, it could be preferable to limit the average of the fluid properties at the OGV/BPD interface to a lower radius, in order for the boundary conditions to be representative of the portion of the flow that the SACOC actually encounters. Figure 12 depicts the Nusselt number obtained while imposing the stagnation pressure averaged over $R \in [0, 1.5H]$, where H is the fin height, and $\Theta \in [-4.5°, 4.5°]$. Despite the Nusselt number still being not only above the average but also above the best exchanging engine fin, the overestimation is limited to around 20%.

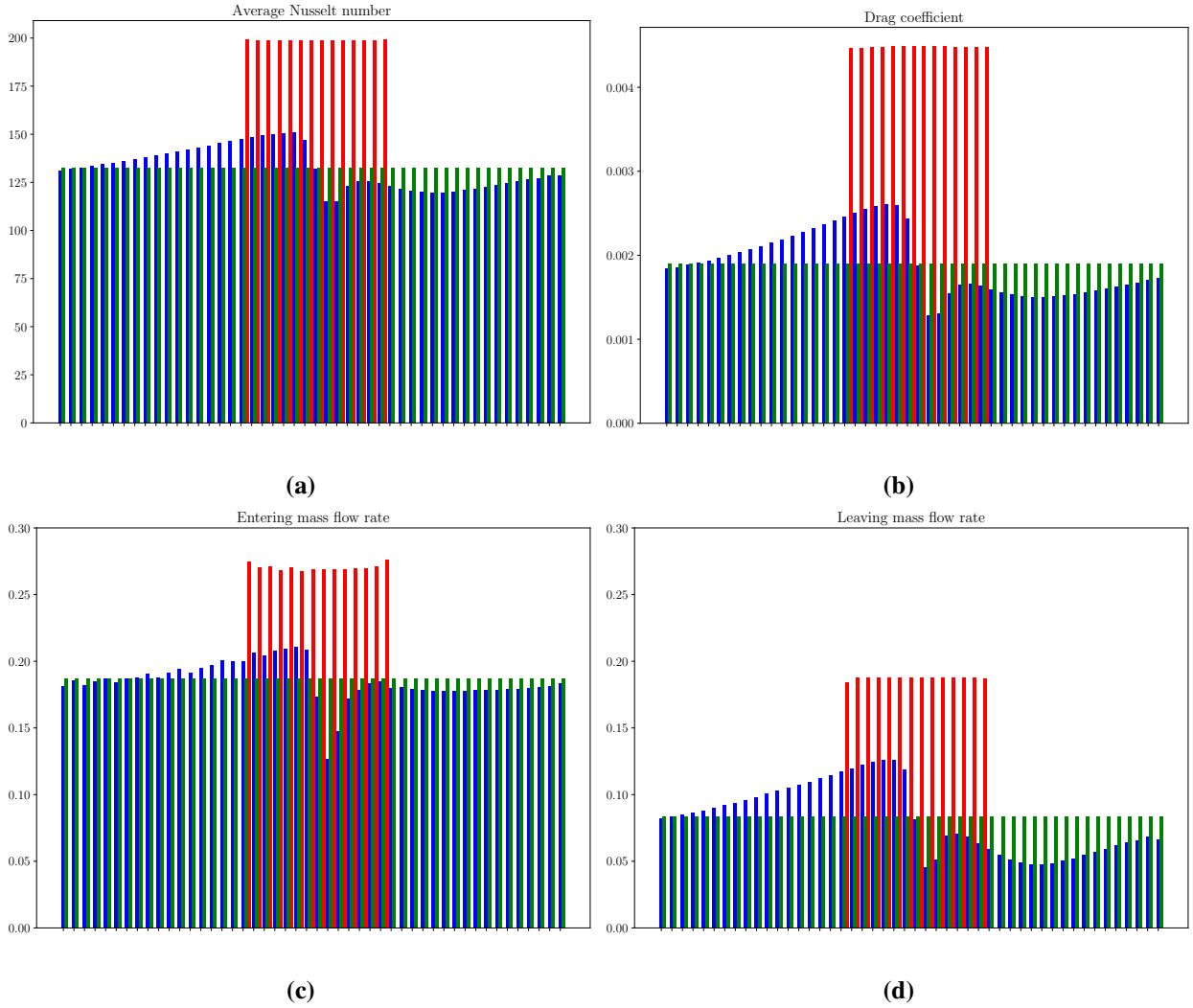

Fig. 11 Uniform boundary conditions. Distribution of average Nusselt number (a), drag coefficient (b), entering (c) and leaving (d) mass flow rate on the SACOC fins: results from engine configuration of §V.A, blue bars; average over SACOC fins of the engine configuration, green bars; results from test bench configuration with uniform boundary conditions, red bars.

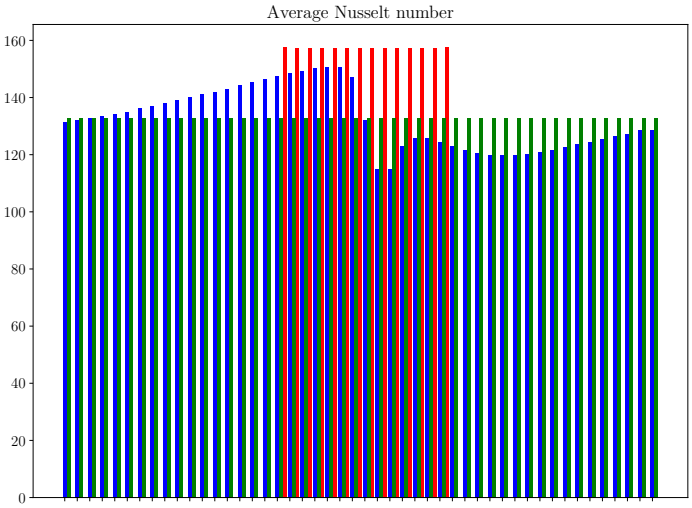

Fig. 12 Uniform boundary conditions, average of boundary conditions limited to $R \in [0, 1.5H]$. Distribution of average Nusselt number. See Fig. 11 for a reference to colors.

2. One-dimensional boundary conditions

At the inlet, one-dimensional profiles of stagnation pressure, stagnation temperature and turbulence are imposed; these profiles are obtained through an azimuthal average at the OGV/BPD interface of the engine configuration; in this case, the pitch and yaw angles of the velocity vector are also averaged and imposed as boundary conditions. Therefore, the direction of the velocity vector at the inlet is not fully axial. Similar boundary conditions, in practice, can be obtained through distortion screens of heterogeneous porosity which, thanks to the pressure drop the flow blockage induces, modify the stagnation pressure profile allowing the reproduction a non-uniform flow (see, for instance, [25]).

Figure 13 shows the comparison between the Mach number profiles at the inlet and at the OGV/BPD interface (averaged along the azimuth Θ). As illustrated, these boundary conditions allow us to recreate the boundary layer seen by the average engine fin.

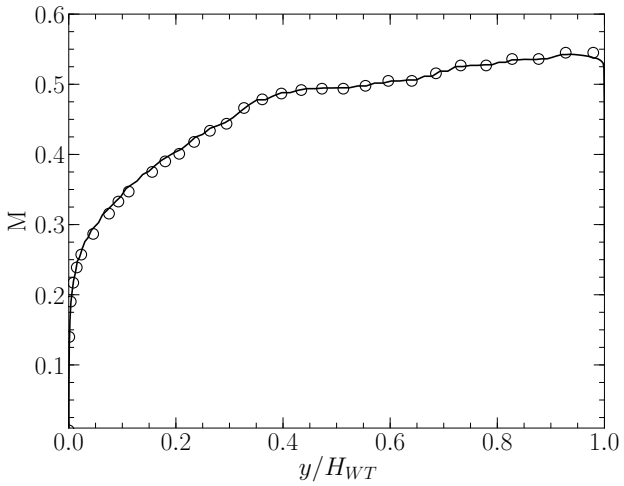

Fig. 13 One-dimensional boundary conditions. Comparison of Mach number profiles: —— wind-tunnel's inlet with one-dimensional boundary conditions; ○ OGV/BPD interface of the engine configuration.

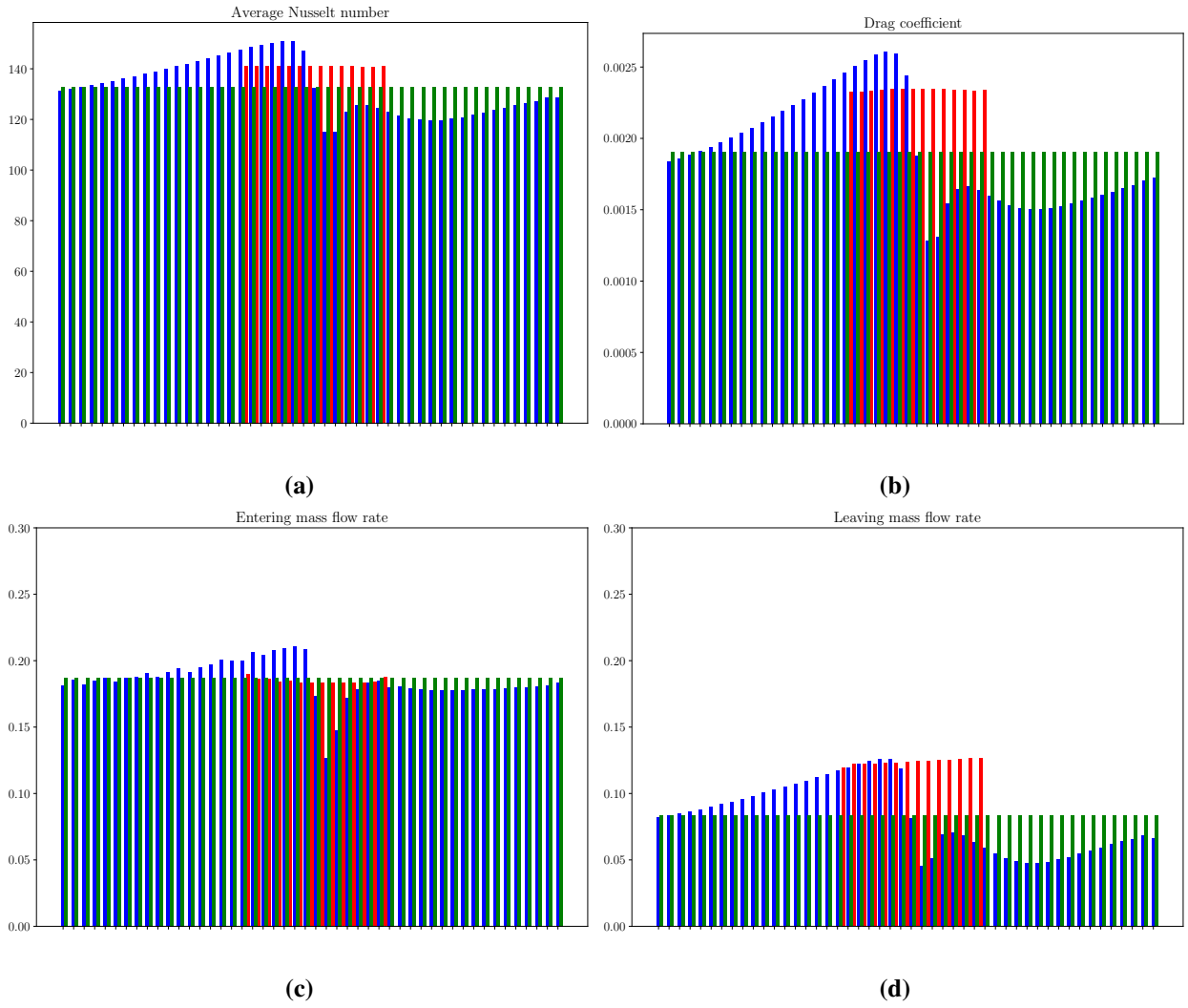

Fig. 14 One-dimensional boundary conditions. Distribution of average Nusselt number (a), drag coefficient (b), entering (c) and leaving (d) mass flow rate on the SACOC fins: blue bars, results from engine configuration of §V.A; green bars, average over SACOC fins of the engine configuration; red bars, results from test bench configuration with one-dimensional boundary conditions.

Figure 14 shows the Nusselt number, drag coefficient and entering as well as leaving mass flow rate for each SACOC fin compared to the results presented in §V.A. All the SACOC fins have a similar behavior (except for some slight differences for the leaving mass flow rate, see Fig. 14d), which, despite the boundary conditions being uniform along the spanwise direction, is not entirely obvious since the entering flow is not axial. The local distribution of the performance parameters of interest is not captured, yet, as can be seen from Fig. 14a, the average Nusselt number is very well predicted with respect to the average engine fin, with an overestimation of around 6%, which is a significant improvement compared to the results obtained with uniform boundary conditions (see §V.B.1). The drag coefficient (see Fig. 14b), on the other hand, is characterised by an over-prediction of around 20%. The overestimation of both the Nusselt number and drag coefficient can be explained by the behavior of the entering and leaving mass flow rate. If the average entering mass flow rate is extremely well predicted (see Fig. 14c), the leaving mass flow is almost 50% higher compared to the average engine fin. Consequently, more flow runs through the length of the SACOC and both the heat exchange and viscous drag are more elevated. These results illustrate the critical role played by the ejection event taking place within the fins and the importance of accurately reproducing it.

The results shown in Fig. 14, as explained at the beginning of the paragraph, are obtained by imposing a one-

dimensional profile for all the inlet fluid properties, *i.e.*, the stagnation pressure, stagnation temperature, turbulence and pitch/yaw velocity angles. So as to understand which profiles are actually fundamental to reproduce in a wind tunnel to obtain accurate results, additional simulations are run where a mix of one-dimensional and uniform boundary conditions are imposed at the inlet. Figure 15 shows the results obtained for the average Nusselt number, where the darkest bars represent the case where all the inlet profiles are one-dimensional (and therefore coincide with the results shown in Fig. 14a) and the lightest bars represent the case where all the boundary conditions are uniform (and therefore coincide with the results shown in Fig. 11a). As can be seen, as long as a one-dimensional profile is imposed for the stagnation pressure, the prediction of the heat exchanged by the SACOC fins does not significantly change regardless of whether the other inlet variables are 1D or 0D.

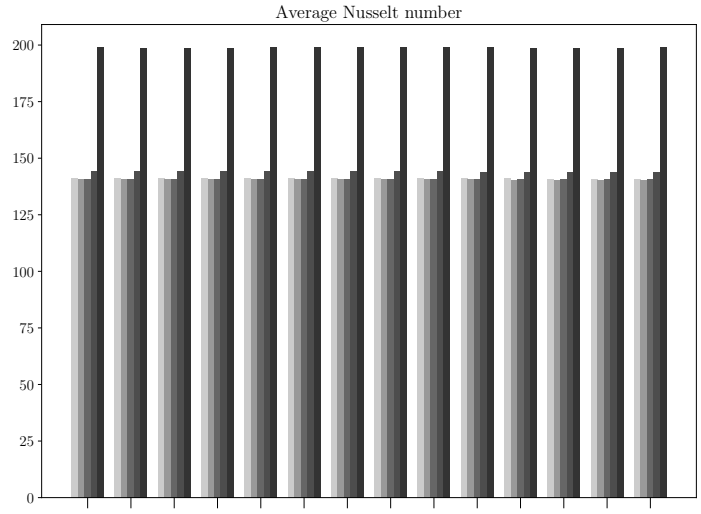

Fig. 15 Mix of uniform and one-dimensional boundary conditions. Distribution of average Nusselt number. From light to dark gray: 1D profiles for all boundary conditions and non-axial flow; same as previous bars but turbulence 0D; same as previous bars but axial flow; same as previous bars but stagnation temperature 0D; 0D profiles for all boundary conditions and axial flow.

Thanks to these results, it is possible to conclude that the complex, anisotropic flow downstream of the OGV described in §V.A can be rather accurately represented by a one-dimensional flow obtained through a circumferential average; the absence of spanwise gradients does not enable to capture the local distribution of the heat exchange observed on the engine fins, yet the behavior of the average SACOC fin is well retrieved. It is also evident how the fluid property that influences the performance parameters the most is the stagnation pressure; indeed, imposing a 1D profile of stagnation pressure at the inlet amounts to injecting a boundary layer; this leads to a good prediction of the mass flow entering the SACOC fins and, therefore, of the global heat exchange; however, the under-prediction of the ejection event taking place within the fins with respect to the engine configuration leads to a slight overestimation. In practice, such boundary conditions are certainly more laborious to recreate compared to a homogeneous flow, yet, as these results show, necessary.

3. Two-dimensional boundary conditions

The two-dimensional cartography of the stagnation pressure, stagnation temperature, turbulence and direction of the velocity vector is extracted from the OGV/BPD interface of the engine and imposed as boundary conditions at the inlet of the wind-tunnel. These boundary conditions recreate the most faithful representation of the engine flow with the given test bench geometry.

In Figure 16 the main performance parameters of the SACOC are compared to the results obtained in §V.A. As can be seen from Fig. 16c, imposing the exact field of stagnation pressure at the inlet leads to a very good prediction of the entering mass flow rate of every fin. Furthermore, the distribution of the Nusselt number and of the drag coefficient resembles that of the engine configuration, with the fins on the left-hand side (*i.e.*, the pressure side in the engine

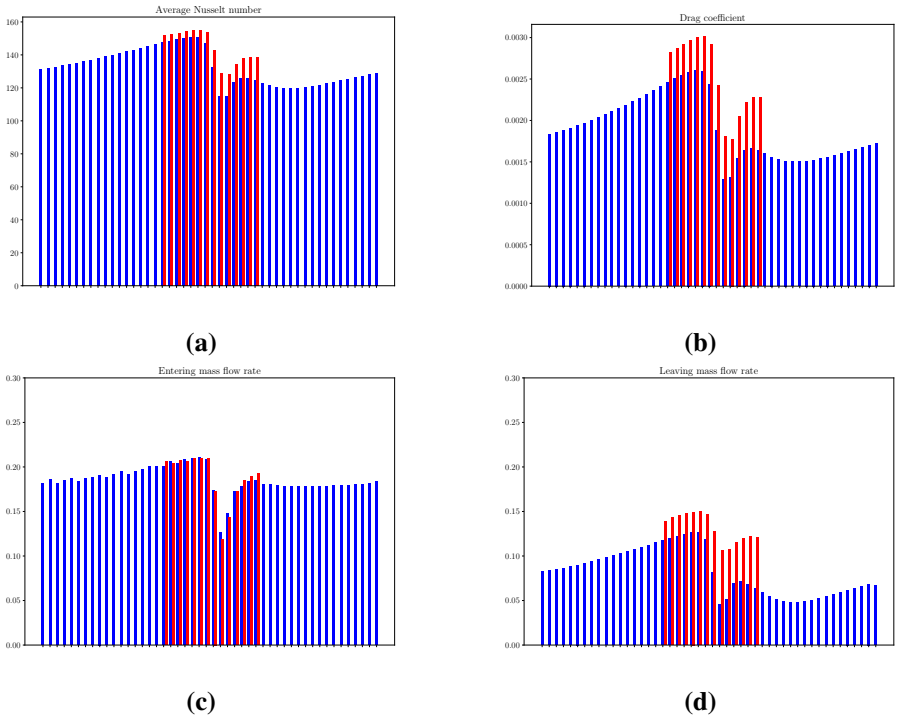

Fig. 16 Two-dimensional boundary conditions. Distribution of average Nusselt number (a), drag coefficient (b), entering (c) and leaving (d) mass flow rate on the SACOC fins: blue bars, results from engine configuration of §V.A; red bars, results from test bench configuration with two-dimensional boundary conditions.

configuration) exchanging more heat and being characterized by a higher viscous drag than the fins on the right-hand side (*i.e.*, the suction side in the engine configuration); on the other hand, a certain level of overestimation can be observed, particularly accentuated for the drag coefficient on the right-hand side fins. This can be explained once again by the distribution of the leaving mass flow rate, which is significantly higher for every SACOC fin compared to the engine configuration; this indicates that despite the representativeness of the boundary conditions, it is extremely arduous to finely reproduce the ejection event observed in the SACOC of the engine configuration.

So as to further investigate the behavior of the flow in the wind tunnel, visualizations of the $\theta = 0.4$ iso-surface and velocity streamlines on the left- and right-hand side of the wind tunnel are given in Fig. 17. The analogous flow visualizations given in Fig. 9 showed how the suction side in the engine configuration is affected by a strong flow separation which explains the higher overall pressure drop and higher mass flow loss of the suction-side fins. As can be seen, the wind tunnel flow has a completely different behavior since no flow separation is observed on the right-hand side of the channel and the only difference between the two sides is the stronger deflection of the velocity streamlines on the right-hand side (Fig. 17b, bottom). Given the precision with which the inflow conditions are prescribed, the difficulties encountered in reproducing the engine flow reveal the limited representativeness of the wind tunnel configuration. Its small size in both the wall-normal and spanwise directions might, for instance, confine the inlet vortex in a much narrower space and thus lead to a weaker interaction with the SACOC; or its limited length in the streamwise direction, at the end of which a uniform static pressure is imposed, might force a premature homogenization of the flow.

Table 3 summarizes the global performance parameters of the SACOC on the left- and right-hand side of the wind tunnel, computed as was done in §V.A for building Table 2. The values of the Nusselt number and drag coefficient for both the left- and right-hand side are higher compared to the engine configuration; this is partly due to the aforementioned over-prediction of these quantities and partly due to the fact that fewer fins are installed in the wind tunnel with respect to the engine. On the other hand, the relative difference between the two sides is close to the one observed between the pressure and suction sides (see Table 2). The same cannot be said about the head losses which, due to the absence of flow separation on the right-hand side, present a significantly lower difference between the two sides with respect to the engine configuration.

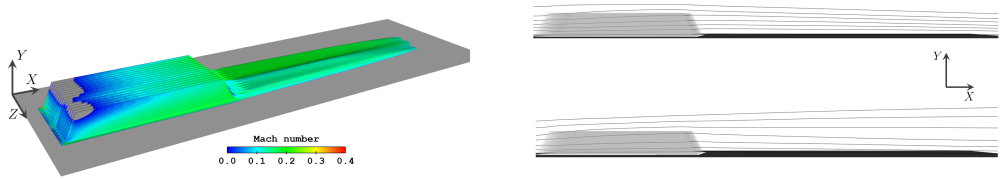

(a) (b)

Fig. 17 Two-dimensional boundary conditions. Temperature iso-surface $\theta = 0.4$ colored by the Mach number (a) and velocity streamlines (b) on the left-hand side (top) and right-hand side (bottom).

Table 3 SACOC's performances in terms of average Nusselt number, drag coefficient and global head losses on the left- and right-hand side of the wind tunnel.

	Left-hand side	Right-hand side	Comparison
$\langle Nu \rangle$	152.32	134.43	+13.3%
C_D	0.0028	0.0021	+38.4%
Head losses	1.05%	1.2%	− 12%

Finally, an additional simulation is performed where the flow is considered to be fully oriented along the streamwise direction X while all the other boundary conditions remain identical. The purpose of the simulation is to assess the impact of the wall-normal and spanwise velocity components on the heat exchange. Figure 18 shows the distribution of the Nusselt number distribution compared to the previous results. As can be seen, the differences with respect to the non-axial flow are very small. These results might corroborate the hypothesis that it is the inflow stagnation pressure which plays the most important role, as seen with the one-dimensional boundary conditions in §V.B.2. On the other hand, given the poor resemblance of the flow downstream of the SACOC with respect to the engine flow even in the case where the exact direction of the velocity vector is imposed at the inlet (see Figs. 9 and 17), the effect of the inflow gyration on the performance of the heat exchanger remains in fact unclear.

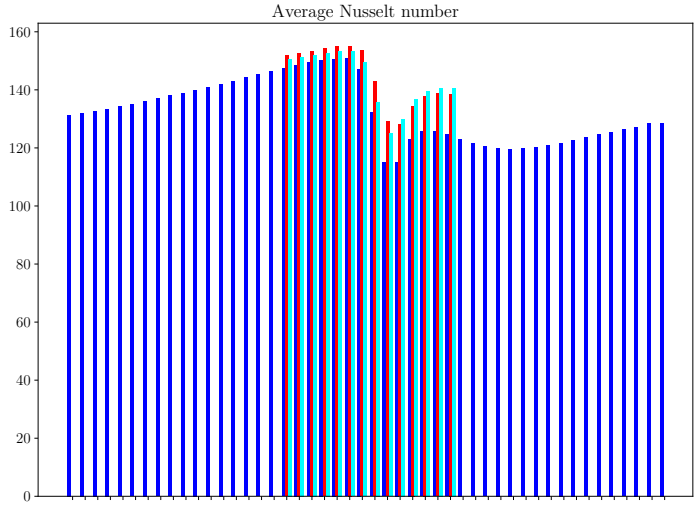

Fig. 18 Two-dimensional boundary conditions. Distribution of average Nusselt number. Blue bars, results from engine configuration of §V.A; red bars, results from test bench configuration with two-dimensional boundary conditions; light blue bars, same as red bars but axial flow.

In conclusion, imposing the exact same flow conditions of the OGV/BPD interface at the inlet leads to a marked improvement in the prediction of all the quantities of interest and allows us to capture certain local effects, such as the asymmetrical distribution of the heat exchange among the different SACOC fins. However other phenomena, such as the strong recirculation zone observed in the engine configuration, have been impossible to reproduce. In practice, these results confirm, on the one hand, the importance of recreating inlet conditions that are representative of the studied flow; on the other hand, they show how the representativeness of a certain configuration is far from being guaranteed by the mere inlet flow conditions and how other limits of the test bench, such as its geometry, have to be taken into consideration.

VI. Conclusion

The conjugate heat transfer analysis of a state-of-the-art surface air-cooled oil cooler (SACOC) of a turbofan aircraft engine is performed in two distinct configurations. The objective is to both identify the main integration effects influencing the performance of the heat exchanger and understand how these effects should be appropriately reproduced in wind tunnel experiments.

The first configuration, set up to meet the first objective, is the by-pass duct of a turbofan engine, where a series of SACOC fins are installed on the OFS just downstream of the OGV. Results show that the flow reaching the heat exchanger is strongly heterogeneous and characterized by residual swirl coming from the fan, two counter-rotating vortexes at the hub and tip of the OGV and an important wake. As a result, the SACOC fins behave differently depending on their position along the OFS, with the pressure-side (resp. suction-side) fins characterized by a higher (resp. lower) heat exchange and viscous drag on their surface. Furthermore, an important flow separation taking place downstream of the SACOC is observed on the suction side which significantly increases the overall pressure drop generated by the heat exchanger. Finally, the fins are affected by an ejection event, more accentuated on the suction side, which leads to an important mass flow loss through the upper part of the SACOC, which reduces the thermal efficiency of the heat exchanger.

The second configuration, relevant to the second objective, is a typical square wind tunnel test rig, where a reduced number of SACOC fins are installed on the lower wall. At the inlet, three different inflow conditions are considered. First, an axial, homogeneous flow representing the surface average of that reaching the SACOC in the engine configuration; very poor predictions are obtained for all quantities of interest since the lack of a representative boundary layer at the inlet leads to the overestimation of both the heat exchange and viscous drag. Second, a one-dimensional flow obtained through a circumferential average of the engine flow; better results are achieved for all quantities even though only the behavior of the average engine SACOC fin is captured due to the lack of spanwise gradients; besides, further investigations show that as long as a one-dimensional profile of stagnation profile is prescribed at the inlet the prediction of the heat exchange and of the viscous drag remains satisfactory regardless of whether the other inflow conditions are homogeneous or not, confirming the criticality of injecting a representative boundary layer. Third, a two-dimensional flow where every fluid property is directly taken from the engine flow; these boundary conditions lead to a considerable improvement of the predictions of all the quantities of interest and some local effects, such as the distribution of the heat exchange among the fins, are captured; on the other hand, certain features of the engine flow, such as the aforementioned mass loss by the upper part of the heat exchanger and the large flow separation taking place downstream of the SACOC on the suction side, are not observed in the wind tunnel, thus revealing the limited representativeness of this configuration.

The study allows us to draw several conclusions. First of all, the interest in analyzing the performances of the SACOC in its operating environment, *i.e.*, the turbofan by-pass duct, has proven to be unquestionably concrete; the effects of the complex flow leaving the OGV on the heat exchanger are strong and need to be taken into consideration in the SACOC design process; in this work, only the effect of the OGV on the SACOC is studied, although it cannot be excluded that investigating the reciprocal, *i.e.*, the effect of the presence of the SACOC on the performance of the OGV, is equally important. Second, it appears from the study that the thermal performance of the heat exchanger is essentially driven, on the one hand, by the mass flow entering at the leading edge and, on the other hand, by the mass flow leaving the SACOC from the upper part without reaching the trailing edge; the study shows that the former is relatively easy to reproduce since it only depends on the inlet stagnation pressure; the latter, on the contrary, seems to depend on features of the flow, such as the flow separation taking place downstream of the SACOC, which are more challenging to recreate. Moreover, the importance in the present case of the inlet flow conditions in wind tunnel experiments has been assessed; as the study showed, satisfactory average results can *a priori* be obtained by injecting a representative one-dimensional boundary layer; this, in practice, can be done with distortion screens. Finally, the study shows that in the present case the accuracy of lower scale experiments does not entirely rest on the inflow conditions and that the representativeness of

the test rig itself needs to be questioned; in other words, increasing the complexity and the fidelity of the inlet flow without increasing those of the test rig does not necessarily guarantee that considerably better results will be obtained.

Acknowledgments

We thank J. Bertucchi of Safran Aircraft Engines for the generation of the meshes used in this work, T. Chantrait of Safran Tech for his help in implementing the aerothermal coupling and T. Hainaut of Safran Aircraft Engines for the fruitful discussions which led to the realization of the engine simulation.

References

[1] Jafari, S., and Nikolaidis, T., "Thermal management systems for civil aircraft engines: Review, challenges and exploring the future," *Applied Sciences*, Vol. 8, No. 11, 2018, p. 2044.

[2] Griffin, J. G., Singer, I. D., and Summers, R. L., "Lubrication cooling system for aircraft engine accessory," , May 1 1979. US Patent 4,151,710.

[3] Schwarz, F. M., and Elsaesser, F. L., "Air-oil heat exchanger," , Mar. 6 2012. US Patent 8,127,828.

[4] Bajusz, D., Cornet, A., Friedel, J., and Raimarckers, N., "Air-oil heat exchanger placed at the location of the air separator nose of a turbojet, and a turbojet including such an air-oil heat exchanger," , Jul. 2 2009. US Patent App. 12/342,206.

[5] Elder, J. S., "Gas turbine engine heat exchanger with tapered fins," , Jul. 22 2014. US Patent 8,784,047.

[6] Kadle, D., and Sparrow, E. M., "Numerical and experimental study of turbulent heat transfer and fluid flow in longitudinal fin arrays," *ASME Journal of Heat Transfer*, Vol. 108, 1986, pp. 16–23.

[7] Jonsson, H., and Moshfegh, B., "Influence of fin spacing, fin thickness and inlet velocity on the performance of plate fin heat sinks under varying bypass conditions using CFD," *International journal of heat exchangers*, Vol. 1, No. 2, 2000, pp. 177–196.

[8] Kim, S., Min, J. K., Ha, M. Y., and Son, C., "Investigation of high-speed bypass effect on the performance of the surface air–oil heat exchanger for an aero engine," *International Journal of Heat and Mass Transfer*, Vol. 77, 2014, pp. 321–334.

[9] Kim, M., Ha, M. Y., and Min, J. K., "A numerical study on various pin–fin shaped surface air–oil heat exchangers for an aero gas-turbine engine," *International Journal of Heat and Mass Transfer*, Vol. 93, 2016, pp. 637–652.

[10] Sparrow, E., Baliga, B., and Patankar, S., "Forced convection heat transfer from a shrouded fin array with and without tip clearance," *ASME Journal of Heat Transfer*, Vol. 100, 1978, pp. 572–579.

[11] Lau, K. S., and Mahajan, R. L., "Effects of tip clearance and fin density on the performance of heat sinks for VLSI packages," *IEEE transactions on components, hybrids, and manufacturing technology*, Vol. 12, No. 4, 1989, pp. 757–765.

[12] Wirtz, R. A., Chen, W., and Zhou, R., "Effect of flow bypass on the performance of longitudinal fin heat sinks," *ASME Journal of Electronic Packaging*, Vol. 116, 1994, pp. 206–211.

[13] Sousa, J., Villafane, L., and Paniagua, G., "Thermal analysis and modeling of surface heat exchangers operating in the transonic regime," *Energy*, Vol. 64, 2014, pp. 961–969.

[14] Villafañe, L., and Paniagua, G., "Aerodynamic impact of finned heat exchangers on transonic flows," *Experimental Thermal and Fluid Science*, Vol. 97, 2018, pp. 223–236.

[15] Cambier, L., and Gazaix, M., "elsA-An efficient object-oriented solution to CFD complexity," *40th AIAA Aerospace Sciences Meeting & Exhibit*, 2002, p. 108.

[16] "Zset : Non-linear material & structure analysis suite." `http://www.zset-software.com`, Accessed: 2020-10-15.

[17] "CWIPI: coupling with interpolation parallel interface." `http://sites.onera.fr/cwipi`, Accessed: 2020-10-15.

[18] Giles, M., "Stability analysis of numerical interface conditions in fluid–structure thermal analysis," *International journal for numerical methods in fluids*, Vol. 25, No. 4, 1997, pp. 421–436.

[19] Errera, M.-P., and Duchaine, F., "Comparative study of coupling coefficients in Dirichlet–Robin procedure for fluid–structure aerothermal simulations," *Journal of Computational Physics*, Vol. 312, 2016, pp. 218–234.

[20] Moretti, R., Errera, M.-P., Couaillier, V., and Feyel, F., "Stability, convergence and optimization of interface treatments in weak and strong thermal fluid-structure interaction," *International Journal of Thermal Sciences*, Vol. 126, 2018, pp. 23–37.

[21] Errera, M.-P., and Chemin, S., "Optimal solutions of numerical interface conditions in fluid–structure thermal analysis," *Journal of Computational Physics*, Vol. 245, 2013, pp. 431–455.

[22] Smith, B., "A near wall model for the k-l two equation turbulence model," *Fluid Dynamics Conference*, 1994, p. 2386.

[23] Dawes, W., "Towards improved throughflow capability: The use of 3D viscous flow solvers in a multistage environment," *Turbo Expo: Power for Land, Sea, and Air*, Vol. 79047, American Society of Mechanical Engineers, 1990, p. V001T01A008.

[24] Dawes, W., "Multi-blade row Navier-Stokes simulations of fan-bypass configurations," *Turbo Expo: Power for Land, Sea, and Air*, Vol. 78989, American Society of Mechanical Engineers, 1991, p. V001T01A060.

[25] Davis, M., Hale, A., and Beale, D., "An argument for enhancement of the current inlet distortion ground test practice for aircraft gas turbine engines," *J. Turbomach.*, Vol. 124, No. 2, 2002, pp. 235–241.